Tracking Metal Electrodeposition Dynamics from Nucleation and Growth of a Single Atom to a Crystalline Nanoparticle

*Haytham E. M. Hussein,† Reinhard J. Maurer,† Houari Amari,⊥ Jonathan J. P. Peters,‡ Lingcong Meng,§ Richard Beanland,‡ Mark E. Newton,‡ and Julie V. Macpherson†**

†Department of Chemistry, University of Warwick, Coventry, CV4 7AL, UK

‡Department of Physics, University of Warwick, Coventry, CV4 7AL, UK

⊥ Department of Mechanical, Materials and Aerospace Engineering, University of Liverpool, L69 3GH

§Department of Chemistry, University of Southampton, SO17 1BJ

*Corresponding author: j.macpherson@warwick.ac.uk

KEYWORDS. Electrodeposition, atom, nanoparticle, gold, boron doped diamond, transmission electron microscopy, identical-location

ABSTRACT. In electrodeposition the key challenge is to obtain better control over nanostructure morphology. Currently, a lack of understanding exists concerning the initial stages of nucleation and growth, which ultimately impact the physicochemical properties of the resulting entities. Using identical location scanning transmission electron microscopy (IL-STEM), with boron doped diamond (BDD) serving as both an electron transparent TEM substrate and electrode, we follow this process, from the formation of an individual atom through to a crystalline nanoparticle, under potential pulsed conditions. In doing so, we reveal the importance of electrochemically driven atom transport, atom cluster formation, cluster progression to a nanoparticle and the mechanism by which neighboring particles interact during growth. Such information will help formulate electrochemical deposition procedures and promote wider uptake of electrodeposited structures in a wide range of societally important applications. This type of measurement is possible in the TEM because the BDD possesses inherent stability, has an extremely high thermal conductivity, is electron beam transparent, free from contamination and robust enough for multiple deposition and imaging cycles. Moreover, the platform can be operated under conditions such that we have confidence that the dynamic atom events we image are truly due to electrochemically driven deposition and no other factors, such as electron beam induced movement.

Electrodeposition, the electrochemically driven formation of solid structures on an electrode surface, has the potential to be a key technology for advancing energy storage and conversion capabilities, aiding in the design of, for example, advanced electrode materials for water splitting, fuel cell technologies and carbon dioxide capture and turnover.[1-3] Many of these applications require precise control over the atomic-scale architecture of the resulting metal structure.[4-5] However, despite the huge technological possibilities, electrochemical deposition strategies have yet to realize their full potential. One decisive factor is related to the fact that surprisingly little is known about the mechanistic details of the initial stages of electrodeposition, at the atom level.[6-8] Such information is crucial if the required control is to be obtained and implemented.

Electrochemically, growth is traditionally treated using either classical or atomistic theories, which describe the process as the formation of supercritical (stable) nuclei, which grow by direct addition of atoms, formed by electroreduction, on the nuclei surface.[9-11] Experimentally, analysis is typically limited to current-time (*i*-*t*) measurements that give average, macroscopic information from which nanoscale behavior is inferred, such as nucleation rate and number of growth nuclei.[9-11] However, studies making use of advancements in microscopic analysis often show that these models are inappropriate descriptors for the early stages of nucleation and growth.[7, 12-16] Such work has led to factors such as electrochemically driven surface diffusion and aggregation being postulated as important pathways,[7, 16] but to date such processes have yet to be dynamically visualized and thus confirmed. Furthermore, the resolution obtained using scanning probe techniques such as atomic force microscopy (AFM) and scanning electrochemical cell microscopy is typically limited to the nanoparticle (NP) level. Electrochemical scanning tunneling microscopy measurements can resolve individual atoms, but studies typically focus on two-dimensional growth and dissolution.[17] Liquid cell transmission electron microscopy (TEM),[18] whilst making

huge strides in monitoring dynamic electrochemical systems,[19] has limited resolution due to factors such as electron scattering in the liquid and electron-beam induced reactions. In contrast, *ex-situ* high resolution aberration corrected scanning TEM (STEM) techniques can not only resolve single atoms, but is able to quantify the number of atoms within a particle.[20]

Our aim is to dynamically visualize in details the earliest stages of nucleation and growth, beginning with the smallest possible electrodeposited entity, a single atom,[21-24] with millisecond temporal resolution. We use identical location (IL)-STEM,[25-26] with repeated electrodepositions and *ex-situ* STEM imaging of the same area, to follow and elucidate these initial stages, effectively taking "snapshots" of the nucleation and growth process at defined time intervals. We also take care to minimize (and quantify) electron beam induced effects. We achieve our overall aim by employing IL-STEM in combination with a TEM substrate made of a conducting boron doped diamond (BDD),[27] that functions as both an electrode and inherently stable electron-transparent support. The BDD brings significant advantages to dual electrode-IL-TEM measurements such as its inherent robustness for repeat measurements, low atomic number, crystallinity, stability, extremely high thermal conductivity and very low Bremsstrahlung backgrounds.[28]

RESULTS and DISCUSSION

Operational Procedure for Monitoring Gold Nucleation and Growth: The BDD electrode-TEM platform was produced by ion milling a thin disc of chemical vapor deposited BDD to electron transparency (shown schematically in Figure 1a); the edge of the ion milled hole is typically less than 35 nm thick, as measured using electron energy loss spectroscopy (EELS). The EELS spectrum of the carbon (C) K ionisation edge in this area is shown in Figure 1b. The C edge at 284 nm indicates sp^3 bonding (i.e. diamond). The thickness of the specimen is determined from the ratio of zero-loss electrons to the total transmitted intensity extracted from the low-loss part of

the spectrum and the mean free electron path in diamond at an electron energy of 200 kV (97.6 nm).[29] A field emission scanning electron microscope (FE-SEM) image of the thinnest part of the BDD electrode surface after ion milling, is shown in Figure 1c, whilst Figure 1d depict an ADF-STEM image of the BDD edge; where the differently doped grains are visible.

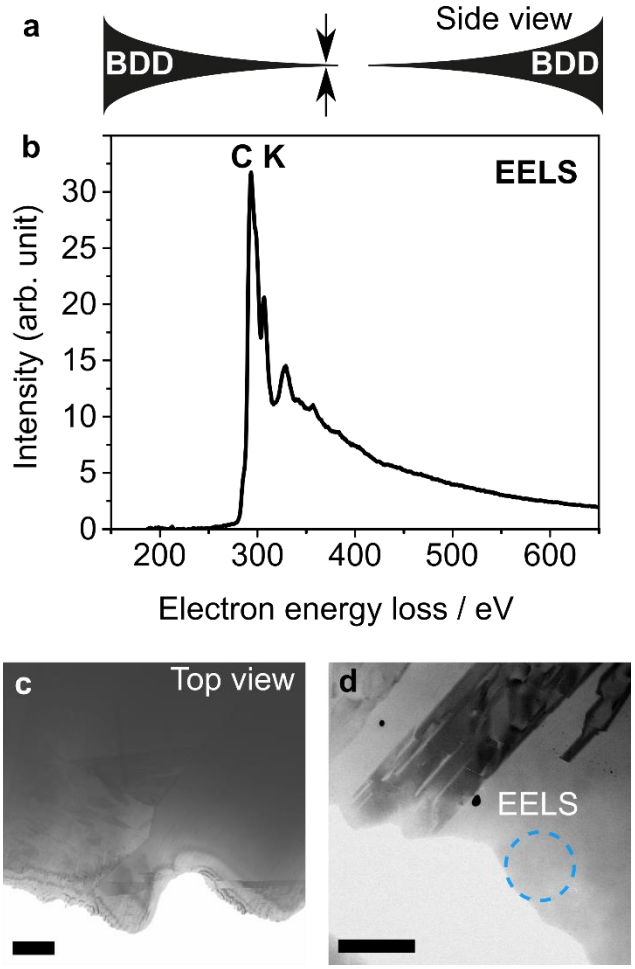

Figure 1. Experimental evidence of the suitability of the BDD electrode for TEM imaging and EELS analysis. (a) Cross-sectional schematic of the BDD-TEM plate after ion milling. (b) EELS of the BDD (on the BDD edge closest to the hole) showing the carbon K ionization edge. (c) FE-SEM image of the thinnest part of the BDD electrode surface after ion milling. (d) Annular dark field-STEM image of the BDD edge; the differently doped grains are visible. Scale bar in c and d, is 100 μm.

Total electrodeposition times of (a) 5 ms, (b) 10 ms and (c) 30 ms, in a solution containing deaerated 1×10^{-3} M $[AuCl_4]^-$ in 0.1 M $HClO_4$ (pH = 1.09), were employed to capture the initial stages of gold (Au) nucleation and growth on BDD. SI 1, Figure S1, Supporting Information, shows the experimental set-up and SI 2, Figure S2 the corresponding cyclic voltammogram for Au^{3+} reduction. Specifically, each experimental cycle leading to a STEM snapshot of nucleation and growth involved: deposition for a defined time period; washing in deionized water; drying; holding at 60 °C for 8 hours under vacuum to eliminate any mobile hydrocarbons; STEM imaging. The first deposition constituted 5 ms, the second a further 5 ms and the third, an additional 20 ms. Note, for the electrode area employed (~0.04 cm^2), as the capacitive current contribution decays in ~ 0.1 ms, 98%, 98% and 99.5% of the currents observed, in the corresponding *i-t* profiles recorded over 0-5 ms, 5-10 ms and 10-30 ms respectively, are due to faradaic processes. The distinctive shape of the edge of the BDD support was used as a reference point to allow imaging of the same area in each cycle. All IL imaging was carried out in annular dark field (ADF)-STEM mode using a fine probe (current 23 pA, convergence semiangle ~25 mrad, 8 μs per pixel), with each area imaged only once per electrodeposition time, unless otherwise stated. A typical sequence of IL-ADF-STEM images from the same area are shown in SI 3, Figure S3. Similar electrodeposition dynamics where observed close to, and up to a radial distance of ~ 500 nm (the limit of the electron beam transparency of the substrate), from the edge of the hole. Further data analysis was carried out by examining selected regions of these and other images.

Electrodeposition of Au was driven at a potential of -0.5 V *vs* a saturated calomel reference electrode (SCE), which equates to an overpotential, η, of -1.2 V. At this potential, a faradaic current contribution for the evolution of hydrogen, on the deposited Au nanostructures, is not expected, based on the data shown in SI 2, Figure S2. Under these conditions, the size of the critical

nucleus, N_c, is calculated to be smaller than a single atom, using the atomistic theory of nucleation.[10, 21, 30] Here the number of atoms in the critical nuclei, N_c, can be determined by examining the dependence of the nucleation rate, J (nuclei cm^{-2} s^{-1}), on η in accordance with Equation 1:[10, 31]

$$\frac{\partial \ln J}{\partial |\eta|} = \frac{-N_c z F}{2.303 R T} \quad (1)$$

where z is the number of electrons involved in the reduction process = 3, F is the Faraday constant (= 96485 C mol^{-1}), R is the gas constant = 8.314 J K^{-1}mol^{-1}, and T is the temperature = 293 K. J was determined from analysis of IL-ADF-STEM images for the same deposition area over three growth periods, 0 to 5 ms, 5 to 10 ms and 10 to 30 ms, (*i.e.* three images in total). This analysis was then performed in two other growth areas, also over the three different time periods, leading to nine images in total analyzed. Three such IL-ADF-STEM images recorded in the same area, are shown in SI 3, Figure S3, which were used to extract the number of Au nuclei on the surface. From the nine analysed images, J and N_c were determined as 1.33×10^{19} cm^{-2} s^{-1} ($\pm 3.6 \times 10^{17}$ cm^{-2} s^{-1}) and 0.14 ± 0.004 atoms, respectively; the latter indicating that single electrodeposited atoms should be stable on the surface. Note, the experimentally measured nucleation densities and J values are orders of magnitude greater than those predicted by analysis of the recorded *i-t* curves using classical growth theories.[7, 13]

Electrochemically Driven Single Atom Motion: After 5 ms (Figures 2a to 2d and SI 3, Figure S3a), the surface contains three distinct electrodeposited structures: isolated, single atoms on the electrode surface (Figures 2a and 2b); clusters (or aggregates) of Au atoms lacking any form of crystallinity that vary in size and number of atoms, which we term atom clusters (ACs, Figure 2c); and particles with crystallinity, typically 1-3 nm in diameter, which we call NPs (Figure 2d). If the

BDD support crystal is aligned to the electron beam, its crystal structure also becomes evident, as shown in Figure 2a, although such conditions were generally avoided to give a clearer view of the deposited Au. This, and other measurements (SI 4, Figure S4) showed that the BDD surface orientation was (110), as expected for CVD polycrystalline BDD growth.[32]

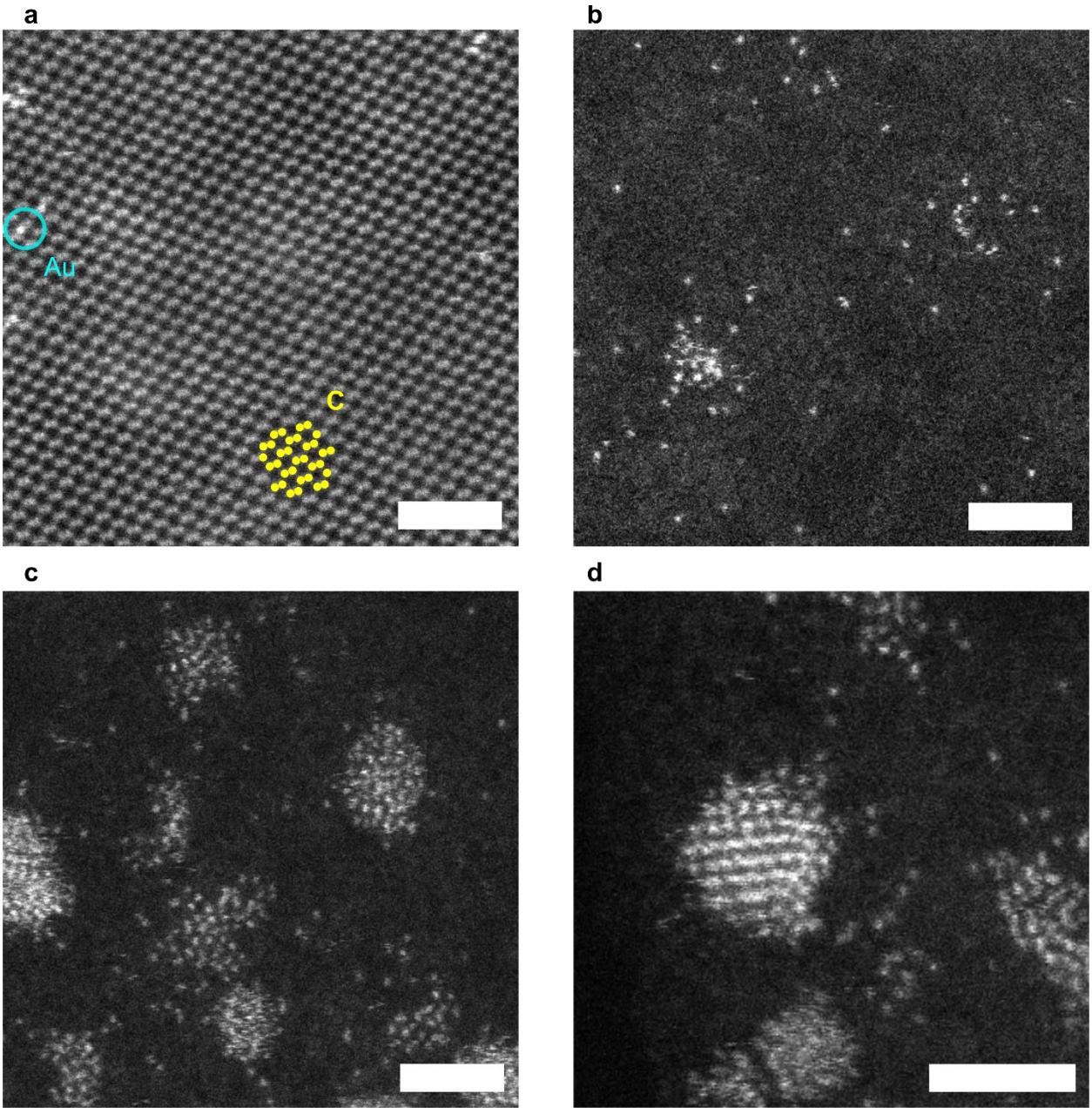

Figure 2. ADF-STEM images of (a) isolated Au atoms (blue circles), and the underlying (110) plane of carbon (C) atoms (pattern structure highlighted in yellow in left hand image) in the BDD TEM platform; (b) isolated Au atoms (c) Au atom clusters and (d) Crystalline Au NPs, electrodeposited on BDD. Scale bar is 2 nm. Electrodeposition was carried out at -0.5 V *vs* SCE for 5 ms.

Although our primary interest is in capturing the dynamics and mechanism of early stage electrodeposition it is first necessary to ascertain whether momentum transfer from the highly energetic (200 kV) electron beam to the particles themselves, induces surface diffusion. Since the largest effect is expected on the least massive particles our focus was on isolated atoms. To separate the effects of electrochemically induced motion from that of the electron beam, we quantified electron-beam induced atom movements for a series of ADF-STEM images recorded at different time intervals in the same area. A representative series of ten ADF-STEM images containing 41 tracked atoms (colored for clarity) as well as a NP that does not change position, is shown in SI 5, Figure S5 and Movie S1. Note each frame receives an electron dose equivalent to that for each time-stamped IL-STEM image, thus the tenth image has received an electron dose ten times the electron dose used per IL-STEM image. The atom movements observed from Frames 1 to 2 and Frames 1 to 10 are also shown in Figures 3a and 3b respectively. After two electron doses, there is negligible movement of any of the atoms (Figure 3a). Even after an excessive ten doses (Figure 3b), 66% of the atoms have moved a mean square displacement of less than 0.1 $Å^2$ (SI 6, Figure S6), whilst the NP changed its orientation. This demonstrates that the effect of the electron beam on isolated atom movement is negligible under the conditions we employ for IL-STEM imaging.

Dispersion-corrected density functional theory (DFT) calculations[33] were also employed to determine the energy required to move isolated Au atoms over the (110) surface of BDD. A fully oxidized (110) surface was modeled. A mixture of ether (C-O-C) and ketone (C=O) groups on the surface were found to be the most energetically favorable configuration, SI 7, Figure S7. Figure 3c depicts the energetic landscape for Au atom motion across the (110) surface; two preferred directions of travel, [$1\bar{1}0$] and [001], were elucidated, with thermal barriers to atom diffusion of 0.16 eV and 0.25 eV respectively. Since a temperature of 60 °C (thermal baking temperature) corresponds to 0.029 eV of thermal energy per atom, movement of atoms on the BDD platform during thermal baking is thus also of minor concern.

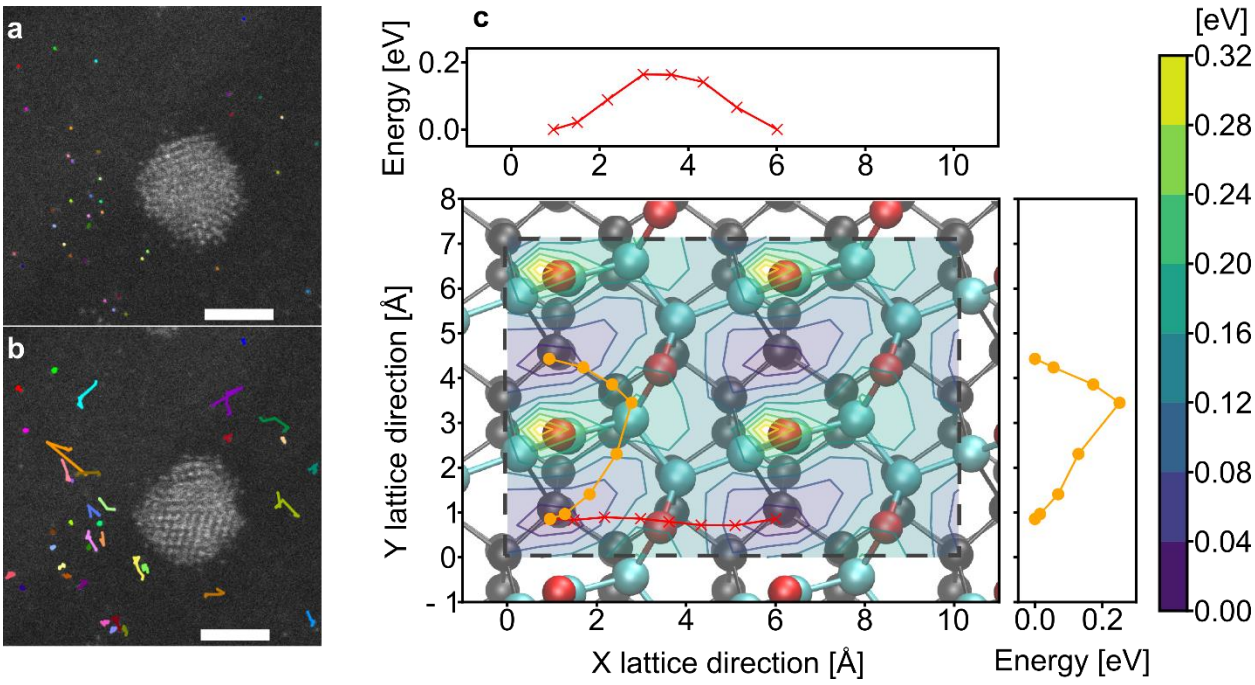

Figure 3. (a and b) Effect of the electron beam on atom mobility. In one location, containing a single NP and 41 atoms (identified by the colored spots), ten consecutive images were recorded. Atom movement from (a) frames 1 to 2 and from (b) frames 1 to 10 is displayed. Scale bar is 2 nm. (c) Energy landscape for adsorption of a single Au atom on an oxidized diamond (110) surface.

Shown is a contour plot with contour energies in eV according to the color bar on the right. The background shows a ball-and-stick model of the surface with carbon atoms in gray, oxygen atoms in red and 1st layer carbon atoms in light blue. Minimum energy barriers along the $[1\bar{1}0]$ (in red) and the [001] (in orange) directions are also depicted.

Importantly, we also find that the Au-BDD-TEM platform is stable over long time periods. Figure S8 shows two images of the same area, the first recorded immediately after the final electrodeposition and the second, 73 days later (stored at room temperature under vacuum). Differences are negligible, even to the extent that individual atoms remain in identical locations.

Early Stage Au Nucleation and Growth from Single Atom to Nanoparticle: Having established the validity of our experiment, we now demonstrate quantitative analysis of early stage Au nucleation and growth using the IL approach in combination with STEM. Quantified analysis of electron scattering is well-established;[34] here we use the contrast of individual Au atoms, together with multi-slice image simulations to calibrate and convert ADF-STEM intensity to a count of Au atoms[34] (see Materials and Methods and SI 9, Figure S9). We first track the effect of an electrochemical deposition potential on the behavior of isolated atoms and ACs. Figure 4 shows representative IL-ADF-STEM images after total deposition times of (a) 5 ms and (b) 10 ms. Six areas of interest are highlighted; squares 1-5 each contain a single AC, whilst square 6 contains isolated atoms. These squares have the same area and sit in the same position in Figures 4a and 4b. The total number of atoms have been counted in each (Table 1).

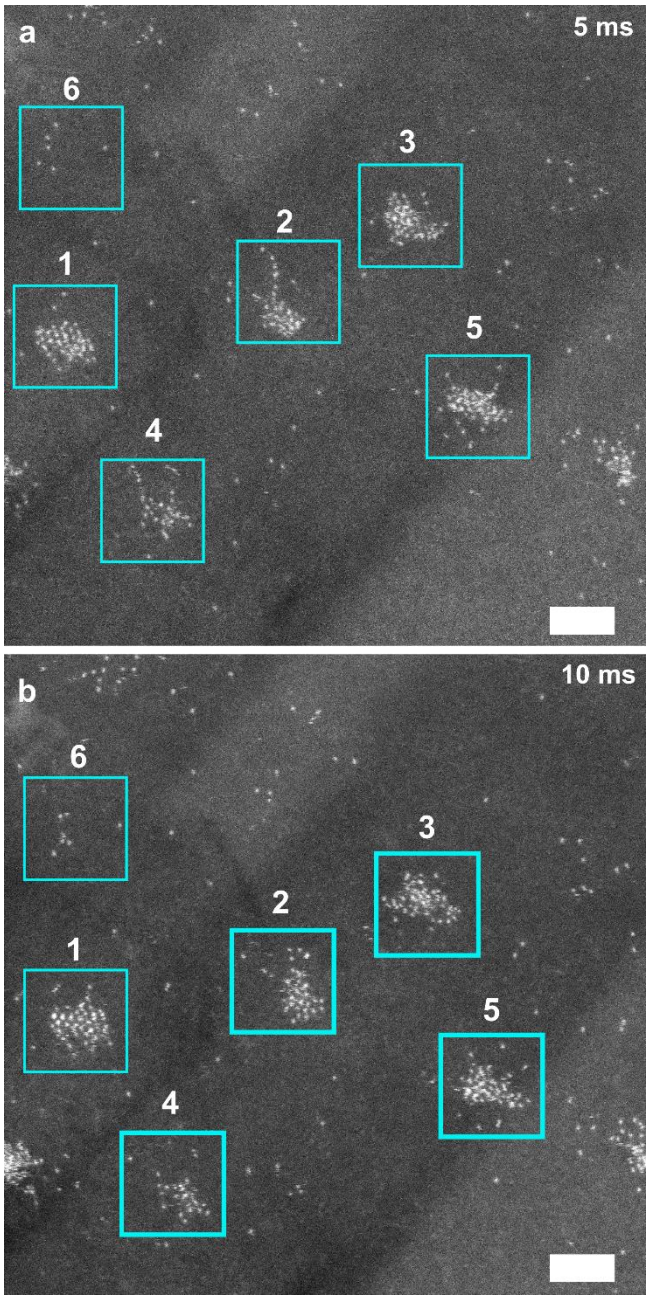

Figure 4. IL-ADF-STEM "snapshot" images of early stage electronucleation and growth focusing on isolated atoms and ACs. (a and b) Show the rearrangement process atoms undergo in response to an applied potential, over 10 ms. Scale bar is 2 nm. Electrodeposition was carried out at -0.5 V *vs* SCE for (a) 5 ms and (b) 10 ms.

Somewhat surprisingly in the 5 ms of electrodeposition between Figures 4a and 4b there does not appear to be any significant change in the atom count of the ACs, in the numbered squares, within experimental error. Although note the total atom count for the whole image does increase from 316 ± 4 atoms (Figure 4a) to 345 ± 3 atoms (Figure 4b). However, what is different is the atoms have changed position, reorganizing themselves, in response to the applied electrode potential. This rearrangement is especially evident in squares 2, 3 and 4 where for the former, square 2, the "line" of six atoms connected to the cluster has now become incorporated into the AC. Since we are confident that our STEM measurement methods do not affect the atom locations significantly, we can also assign the rearrangement of individual atoms towards each other in square 6, as a result of the applied potential.

A second example of electrochemically driven atomic rearrangement is shown in Figures 5a to 5c (and at lower magnification in SI 10, Figure S10). The NP identified with a blue circle acts as a reference point. The highlighted AC (blue square) does not change its total number of atoms in Figures 5a and 5b (160 ± 10 *vs* 160 ± 20 atoms) however, the position of the atoms has clearly changed as the system moves to adopt a lower energy configuration (perimeter of AC also decreased from 3.37 nm to 3.01 nm). After a further 20 ms of applied potential, Figure 5c, the AC transforms into a smaller and more ordered NP (see inset) comprised of only 82 ± 7 atoms (perimeter 1.39 nm). The AC upon converting to a more stable NP has actually lost atoms (although their final location is unclear from these images). Such phenomena have not been considered in the electrodeposition literature and is certainly not currently predicted by any electrodeposition theory. Figure 5 thus not only demonstrates the level of detail IL-ADF-STEM can reveal on early stage growth using the BDD-TEM platforms but enables the elucidation of mechanisms and growth pathways previously not described at the atomic level.

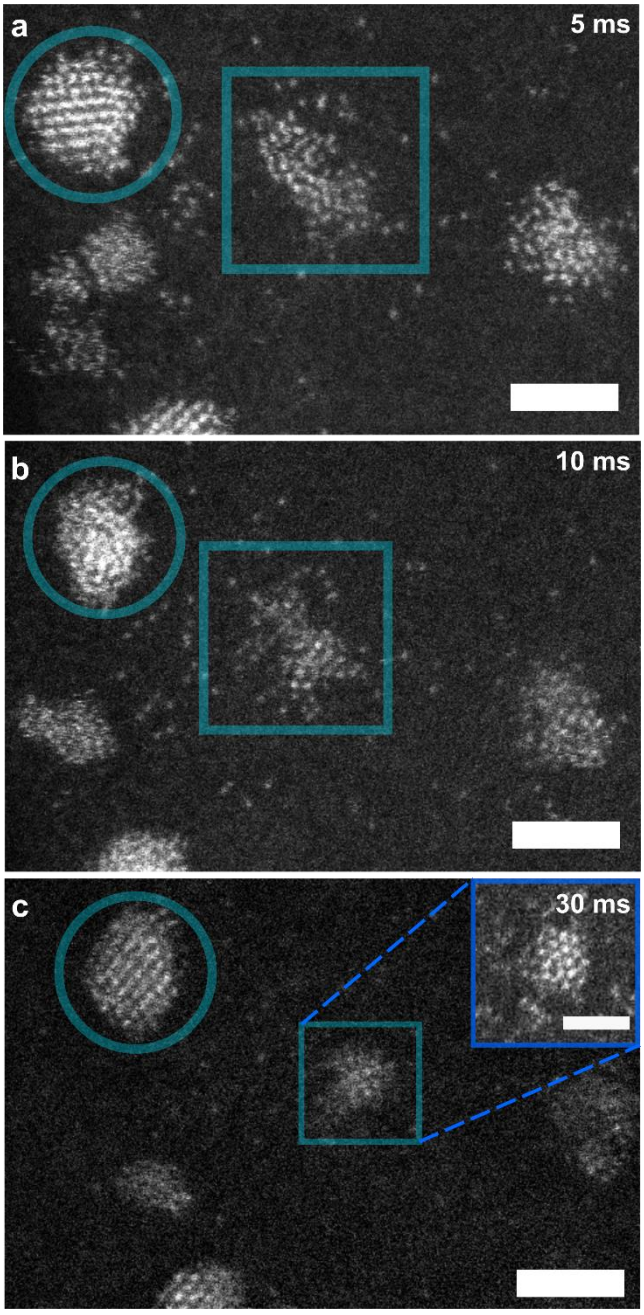

Figure 5. IL-ADF-STEM "snapshot" images of early stage electronucleation and growth focusing on isolated atoms, AC and NP. (a to c) One example of how a NP forms from an AC over a 30 ms electrodeposition time period. Scale bar is 2 nm. Electrodeposition was carried out by applying -0.5 V *vs* SCE for (a) 5 ms (b) 10 ms and (c) 30 ms.

Growth Interactions Between Neighboring ACs and NPs: Also of considerable interest is how neighboring entities (ACs and NPs) interact. We have shown single atoms aggregating into ACs and ACs converting to NPs but have yet to discuss possible interactions between ACs and NPs. The images as shown in Figure S3 provide a wealth of "snapshot" data from which such information can be obtained, as illustrated by Figures 6a to 6c, which show a series of electrodeposition dynamics from three different locations. In Figure 6a at 5 ms, two dominant features are present, a crystalline NP (269 ± 9 atoms) and a disordered AC (153 ± 5 atoms). After a further 5 ms of growth the almost complete disassembly of the AC has occurred via streams of atoms into the NP, which move across both the surface and each other. In response, the NP has become disordered, with clearly not enough time for recrystallization. After a further 20 ms, atom movement is complete resulting in the formation of one single crystalline NP (730 ± 30 atoms), with the surrounding area now devoid of isolated atoms. The size of the NP indicates that during growth not only did the NP incorporate all atoms from the neighboring AC but also incorporated atoms from other sources, most likely due to direct attachment i.e. by direct reduction of Au ions to Au atoms at the NP surface.

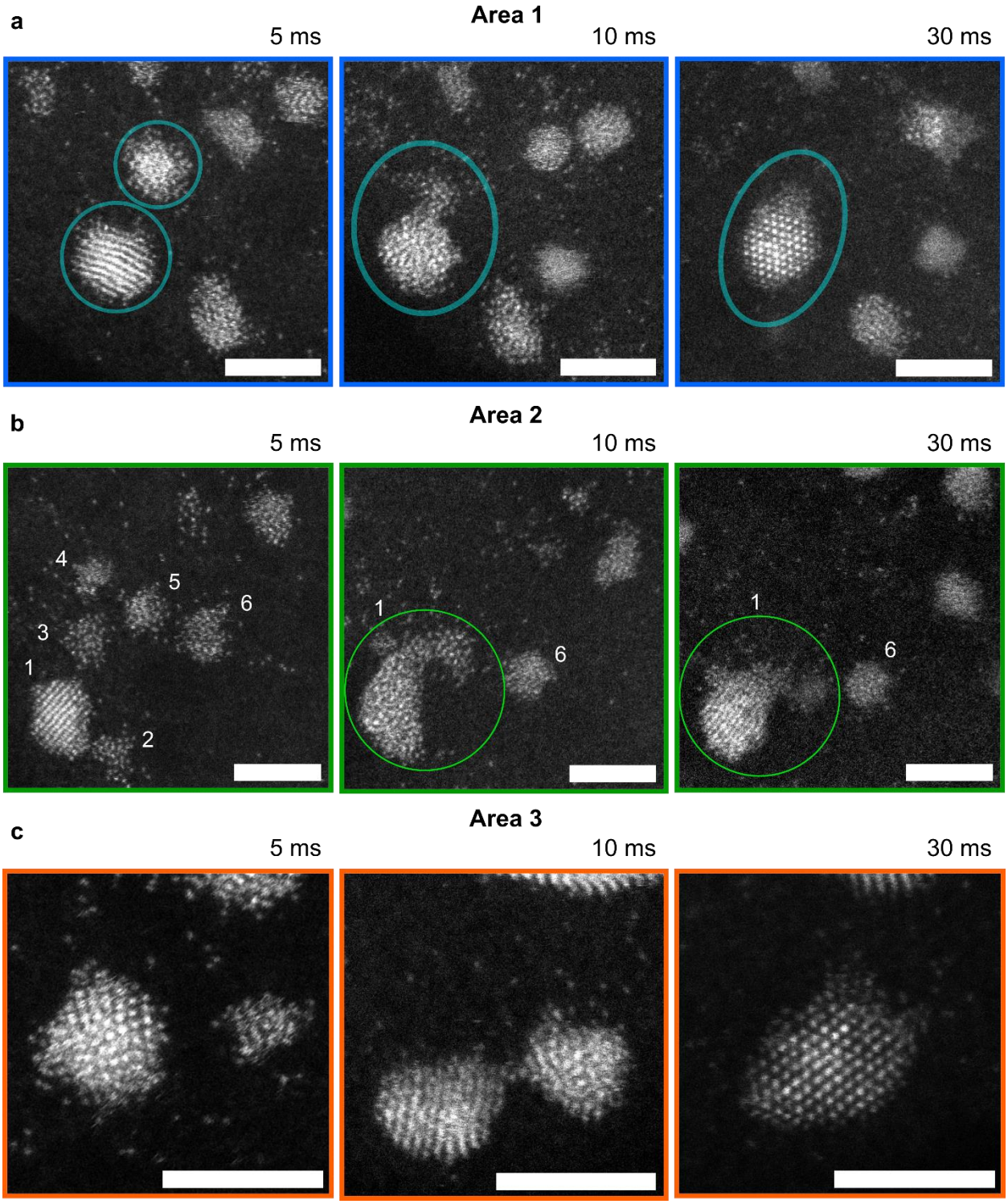

Figure 6. IL-ADF-STEM images of atomic cluster – NP dynamic interactions during electrodeposition. (a to c) AC and NP interactions during Au electrodeposition in three different

areas for "snapshot" growth times of 5 ms, 10 ms and 30 ms at an electrodeposition potential of -0.5 V *vs* SCE. ACs dissemble to provide atoms to a neighbouring crystalline NP, which becomes disordered as a result, followed by recrystallization. Scale bar is 3 nm.

Figure 6b features a monocrystalline Au NP (labelled 1, 222 ± 7 atoms at 5 ms), surrounded by five ACs, (2, 3, 4, 5, 6) with atom sizes of (34 ± 1; 40 ± 1; 35 ± 1; 48 ± 2 and 59 ± 2) respectively. After a further 5 ms, the nearest AC (AC 2) has already been incorporated into NP 1, while ACs 3, 4 and 5 undergo movement and disassembly to provide streams of atoms which also feed into NP 1. This process causes NP 1 to lose crystallinity and become disordered (atom count = 710 ± 30 atoms). This size cannot be accounted for by only considering AC incorporation and again indicates direct atom attachment (from solution). AC 6 does not take part in the disassembly process but instead grows in size to 127 ± 5 atoms, itself becoming a crystalline NP.

This is an example of an AC progressing to a crystalline NP structure by increasing in atom number, in contrast to the data in Figures 5a to 5c. One difference is the fact that AC 6 in Figure 6b is clearly more spherical in nature than the AC captured in the Figure 5 "snapshot". Our data thus indicates that ACs, dependent on their stage of morphological evolution, will either gain or lose atoms during a rearrangement process in their progression to become crystalline. After 30 ms, integration of AC's 3, 4 and 5 into NP 1 is almost complete, with NP 1 reordering into a crystalline structure of size 650 ± 30 atoms. The NP which was AC 6, after a further 20 ms electrodeposition has an atom count of 115 ± 5 atoms, suggesting it has not grown in size during this period. Figures 6a and 6b clearly show that on this timescale, ACs and NPs cannot be considered non-interacting, contrary to classical theories.[11] They also demonstrate that a traditional definition of aggregation where two particles or clusters move across the surface to come together is not strictly true here.

Rather, if there is a suitable distance between NP and AC, it is the disordered AC which loses atoms to the more stable crystalline NP. Whilst this process happens, the NP becomes liquid-like (disordered) and only recrystallizes once the process has (almost) fully completed.

Integration of many ACs into one dominant structure will have implications on the final structure of the NP *e.g.* by creating faults, twin boundaries, defects or leading to irregular structures; all features which can greatly impact the electrocatalytic activity of Au NPs.[35] It is also interesting to consider whether what we observe falls under the definition of electrochemical Ostwald ripening, where less stable particles dissolve to provide atoms for growth of the larger, more stable particle.[36] Here, we observe the more stable NP grow at the expense of the less stable AC, however it is not a dissolution event, whereby atoms from the AC dissolve and directly redeposit into the crystalline NP. Thus we speculate we are witnessing either, what we term "surface mediated" Ostwald ripening, where the supercritical atoms do not dissolve but simply translate from one site to another,[37] or coalescence followed by recrystallization.

Figure 6c presents further information on this process, again showing the interaction between a NP and an AC. After 5 ms electrodeposition, Figure 6c (5 ms), the NP (290 ± 20 atoms) and AC (50 ± 3 atoms) are located within ~ 1.62 nm of each other (face to face). After a further 5 ms electrodeposition, Figure 6c (10 ms), it is only the AC that has significantly taken on atoms (from neighboring sources or *via* direct attachment), growing in size to 220 ± 10 atoms; in doing so the face to face separation has reduced to ~ 0.77 nm and an atom bridge linking the two structures is now evident. The NP has remained fairly consistent in size, 260 ± 10 atoms. After a further 20 ms of growth, one crystalline NP remains (450 ± 20 atoms), Figure 6c (30 ms). Given the atom count, this NP is unlikely to have gained atoms through direct attachment, but as a consequence of atom transfer from AC to NP.

CONCLUSIONS

Our results, using IL-STEM in conjunction with BDD TEM electrodes, provides a tantalizing atom-level insight into the mechanistic dynamics of early stage metal nucleation and growth, the results of which are not described by classical electrodeposition theories. Such knowledge can lead to better control of electrodeposition morphology and the creation of electrochemical deposition methods. We show direct evidence for potential-induced atom movement, atom clustering and cluster transformation, into crystalline NPs, possible *via* both gain or loss of atoms. Discrete entities are also shown to be interactive with a clear tendency for disordered clusters to be consumed within a closely spaced NP, *via* a cluster disintegration process which sees the NP transition through a disordered state first. More wide ranging, the electrochemical production of stable isolated metal atoms on the BDD platform holds considerable promise for single atoms studies in *e.g.* electrocatalysis[38] and magnetism.[39] Finally, the universality of the approach means this technology can reveal the atomic-scale intricacies of a myriad of technologically important electrochemical processes[40] which undergo a morphological change with applied potential.

MATERIALS and METHODS

Solutions: Au electrochemical deposition solutions were prepared from potassium tetrachloroaurate (KAuCl4, 99.99%, Sigma-Aldrich) with perchloric acid (HClO4, 99.99%, Sigma Aldrich) as a supporting electrolyte in ultra-pure Milli-Q water (18.2 MΩ cm, Millipore Corp., U.S.) at 20 °C. All chemicals were used as received without further purification. Au^{3+} deposition solutions contained 1×10^{-3} M $[AuCl_4]^-$ in 0.1 M $HClO_4$ (pH = 1.09) which was deaerated with Argon (Ar) for 20 minutes before electrodeposition to exclude oxygen. Ar flow was maintained over the solution during the experiment.

Materials and Electrode Fabrication: The experiments were performed using a freestanding microcrystalline BDD plate, suitably doped for electrochemical studies (boron dopant level of ~3 $\times 10^{20}$ B atoms cm-3)[27, 41] and grown using microwave chemical vapor deposition (Element Six, Harwell, Oxford).[27] The plate was mechanically polished to ~ 50 μm thickness, with both sides showing a surface roughness of *ca.* 0.18 nm, measured using AFM on the surface of a grain (grain size *ca.* 2-8 μm). The plate was cut into disks of diameter 3 mm (suitable for insertion into the TEM holder) using laser micromachining and acid cleaned to remove machining debris. The plates were Ar^+ ion milled to electron transparency at an accelerating voltage of 6 kV and an angle of incidence of ~4°. The sample was mounted on a post support using glycolphthalate bonding wax (Agar Scientific) allowing continuous milling as the sample rotated. Each side was milled in turn (approx. 2 hours each side) until a small hole (*ca.* 100-300 μm in diameter) was formed in the center of the BDD disk. The disk was mounted into a clamp support for a final low energy ion mill of both sides of the disk at an accelerating voltage of 2 kV with a modulated ion beam, for 30 minutes, to provide a smooth surface finish. The BDD was acid cleaned after ion milling (0.1 M HNO_3 followed by 0.1 M H_2SO_4). To make an ohmic contact to the electrode the upper quarter of one of the edges was sputtered (Moorfield MiniLab 060 Platform) with Ti (20 nm)/Au (400 nm) and annealed in a tube furnace for 5 hours at 450 °C.[27, 42]

Electrochemical Measurements: All electrochemical experiments were carried out using a three-electrode set-up controlled by a potentiostat (CHI730A, CH Instruments, Inc. Austin, TX). A commercial SCE was used as the reference electrode and a helical Pt wire served as the counter electrode. The BDD electrode was electrically connected using a fine metal clamp attached to the Au contact. The disk was dipped into the electrolyte solution using a manual *x,y,z* micropositioner (Newport, Oxford) such that the central hole was in the solution but the Au contact remained dry.

The set-up is shown in Figure S1. Immediately after Au deposition, the grid was rinsed with deoxygenated ultra-pure water and left to dry in a desiccator under an Ar atmosphere, and then stored under vacuum at 60 ^{o}C before transfer to the TEM. Electrodeposition snapshots were recorded for growth periods 0 to 5 ms (5 ms total nucleation and growth), 5 to 10 ms (10 ms total nucleation and growth) and 10 to 30 ms (30 ms total nucleation and growth).

Surface characterization: FE-SEM: FE-SEM was used to image the BDD platform before and after ion milling and also to obtain low magnification images of the Au particles after electrochemical deposition. FE-SEM images were recorded using the In-lens and STEM detector on a Zeiss Gemini operating at 15 kV and 25 kV, respectively (Figure S1). AFM: AFM was employed to measure the roughness of the surface before and after ion milling, AFM images were acquired at a low scan rate (0.25 Hz) in intermittent contact (tapping mode) using a Bruker Innova AFM. TEM: For examining the suitability of BDD TEM supports for imaging and diffraction, TEM characterization was carried out on the BDD platform using a JEOL-JEM 2100 (LaB_6) microscope at 200 kV. The time dependent study of particle shape, structure, size, composition and evolution, during electrochemical nucleation and growth, were investigated by IL-ADF-STEM in a double aberration corrected JEOL JEM-ARM200F at 200 kV. Although deposition occurred on both sides of the platform, images were all taken from the same face. ADF-STEM images were obtained using a JEOL annular field detector with a fine-imaging probe, and a current of 23 pA with a convergence semi-angle of ~25 mrad and an ADF detector inner angle of 50 mrad. EELS: EELS was recorded on a JEOL JEM-ARM200F microscope operating at 200 kV with a Gatan GIF Quantum SE spectrometer. Measurements were performed at a total energy resolution of 3 eV, determined by measuring the full width at half-maximum (FWHM) of the zero-loss peak. The following conditions were chosen for the EELS spectra acquisition: convergence semi-angle

29 mrad, collection semi-angle 100 mrad, exposure time 0.05 s, dispersion 0.5 eV/ch and probe size <0.1 nm.

DFT simulations: All DFT calculations were carried out with the all-electron, numerical atomic orbital code FHIaims[33] using tight integration settings and geometry optimizations down to a force threshold of 0.01 eV per Å. Dispersion corrected functional Perdew-Burke-Enzerhof (PBE) and long-range Van-der-Waals correction (derived by Tkatchenko and Scheffler)[43-44] was employed. Barrier searches were performed using the Atomic Simulation Environment (ASE)[45] and the Climbing Image Nudged Elastic Band (NEB) procedure[46] with a threshold of 0.07 eV per Å. Global geometry optimizations were performed using ASE and the Minima Hopping method.[47-48] The diamond (110) model surface was built using the optimized PBE lattice constant of 3.572 Å. The model is composed of 7 carbon layers and a vacuum orthogonal to the [110] direction of 32 Å. We model the experimental conditions by oxygen passivation of the surface at the top and bottom termination of the surface slab. Upon studying a variety of different possible oxygen functionalization using local and global optimization, we find the most stable surface to be represented by a reconstructed (2×1) surface unit cell of diamond (110) with 2 adsorbed oxygen atoms at the surface (see Figure 4 and Figure S7). Both of them are adsorbed at the top carbon atoms, one as a double bonded ketone (C=O) group, the other one as an ether (O-C-O) group bridging across the (110) carbon ridges.

The two-dimensional energy landscape reported in Figure 3c was calculated using constrained local optimization, where a single gold atom was placed on the oxygen functionalized surface and only allowed to relax vertically. Based on this landscape, climbing image NEB calculations were performed to calculate the two barriers of gold adatom diffusion along the C-C ridges [$1\bar{1}0$] and perpendicular to the ridges [001].

Atom counting procedure from STEM images: The signal from ADF STEM imaging is given as an arbitrary intensity and the objective is to calibrate this to give the number of atoms.[34] Due to the high density of distinct, individual gold atoms surrounding the larger nanoclusters, it is possible to obtain a measure of the intensity from one gold atom. Through comparison to simulations, this single atom intensity can be used to create a calibration curve from ADF intensity to the number of atoms in a vertical column, Figure S9. In measuring the intensity of the gold atoms, first the gold signal must be separated from the background BDD signal. On simple images, this can be sensibly approximated as a plane to be subtracted. However, for images with complicated background intensities, the background is calculated by masking the gold signal and infilling using interpolation (provided by MATLAB®'s *region-fill*). To remove the influence of noise when interpolating, a median and Gaussian filter is applied (with standard deviation of 0.017 nm and window size of 0.2 nm respectively). The intensity of a single atom is then obtained from averaging over a large number of single atoms (typically >100) and the uncertainty is measured as the standard error of the means.

Simulations were performed using QSTEM with 001 orientation gold with a column thickness ranging from 1-60 gold atoms. The microscope parameters used in the simulation were empirically determined from the microscope (200 kV accelerating voltage, detector radius 45-100 mrad, convergence angle of 25 mrad, spherical aberration 1 μm) and with 30 thermal diffuse scattering configurations. The total gold column intensity was then summed and fitted using a parabola. Note that the intensity has discontinuities due to channeling effects.

TABLE 1. Number of atoms in each atom cluster and associated error as function of electrodeposition time for the images presented in Figure 4a (5 ms) and 4b (10 ms).

AC	5 ms (atoms)	10 ms (atoms)
1	57 ± 5	64 ± 4
2	29 ± 4	24 ± 3
3	46 ± 6	50 ± 4
4	65 ±6	57 ± 4
5	57 ± 6	59 ± 3
6	7	7

ASSOCIATED CONTENT

Supporting Information. The following files are available as a PDF free of charge (S1- S10). SI 1. Experimental set-up for metal deposition at BDD-TEM electrode. SI 2. Cyclic voltammogram for gold reduction and stripping at the BDD-TEM electrode. SI 3. Three IL-ADF-STEM images in the same area obtained at electrodeposition times of 5 ms, 10 ms and 30 ms. SI 4. TEM image showing crystallography of the BDD-TEM electrode. SI 5. Atom tracking of atom movement (for 41 atoms) over a ten frame period. SI 6. Statistical analysis of atom movement. SI 7. Ball-and-stick models of the global energy minimum of an oxidized diamond (110) surface slab. SI 8. IL-ADF-STEM images showing the same Au-BDD-TEM platform, 73 days apart. SI 9. Simulation to enable quantification of Au atom numbers from STEM images. SI 10. Low magnification IL-ADF-STEM image of tracked nucleation and growth of Au entities over a growth period of 30 ms.

Movie S1 (available as avi). A 10 s movie comprising the ten ADF-STEM frames displayed in Movie S1 showing the effect of longer time exposure of the electron beam on the movement of Au atoms on the BDD surface.

AUTHOR INFORMATION

Corresponding Author

*j.macpherson@warwick.ac.uk

ORCID

Author Contributions

The manuscript was written through contributions of all authors. All authors have given approval to the final version of the manuscript. H.E.M.H and J.V.M devised the concept of BDD platforms for IL-STEM monitoring of electronucleation. H.E.M.H and L.M. carried out the initial experiments. H.E.M.H and H.A carried out the IL-STEM imaging. H.E.M.H and R.B prepared the BDD substrates. H.E.M.H ran the electrodeposition experiments. H.E.M.H, R.B, H.A., J.J.P.P, M.E.N, R.J.M and J.V.M were involved in analysis of the data. R.J.M performed the DFT simulations. H.E.M.H and J.V.M wrote the manuscript with input from authors.

Notes

Authors declare no competing financial interests.

Funding Sources

This work was supported by the Royal Society (INF/R1/180026), EPSRC (EP/N035437/1, EP/P031544/1), AstraZeneca and the University of Warwick. JVM gratefully acknowledges the Royal Society for an Industry Fellowship. Computing facilities were provided by the University of Warwick and HPC Midlands (EP/P020232/1).

ACKNOWLEDGMENT

The authors would also like to thank Prof. Patrick Unwin, Dr. Cameron Bentley (Department of Chemistry, University of Warwick) and Prof. Philip Bartlett (Department of Chemistry, Southampton University) for helpful comments during preparation of the manuscript. We also

thank Mareike Herrmann (Department of Chemistry, University of Warwick) for laser cutting and ohmically contacting the BDD TEM disks.

REFERENCES

(1) Mariano, R. G.; McKelvey, K.; White, H. S.; Kanan, M. W., Selective Increase in CO_2 Electroreduction Activity at Grain-Boundary Surface Terminations. *Science* **2017,** *358*, 1187-1192.
(2) Kim, T. W.; Choi, K. S., Nanoporous $BiVO_4$ Photoanodes with Dual-Layer Oxygen Evolution Catalysts for Solar Water Splitting. *Science* **2014,** *343*, 990-996.
(3) Wang, C.; Waje, M.; Wang, X.; Tang, J. M.; Haddon, R. C.; Yan, Proton Exchange Membrane Fuel Cells with Carbon Nanotube Based Electrodes. *Nano Lett.* **2004,** *4*, 345-348.
(4) Zach, M. P.; Ng, K. H.; Penner, R. M., Molybdenum Nanowires by Electrodeposition. *Science* **2000,** *290*, 2120-2123.
(5) Li, M.; Zhao, Z.; Cheng, T.; Fortunelli, A.; Chen, C.-Y.; Yu, R.; Zhang, Q.; Gu, L.; Merinov, B. V.; Lin, Z.; Zhu, E.; Yu, T.; Jia, Q.; Guo, J.; Zhang, L.; Goddard, W. A.; Huang, Y.; Duan, X., Ultrafine Jagged Platinum Nanowires Enable Ultrahigh Mass Activity for the Oxygen Reduction Reaction. *Science* **2016,** *354*, 1414-1419.
(6) Valov, I.; Sapezanskaia, I.; Nayak, A.; Tsuruoka, T.; Bredow, T.; Hasegawa, T.; Staikov, G.; Aono, M.; Waser, R., Atomically Controlled Electrochemical Nucleation at Superionic Solid Electrolyte Surfaces. *Nat. Mater.* **2012,** *11*, 530-535.
(7) Ustarroz, J.; Hammons, J. A.; Altantzis, T.; Hubin, A.; Bals, S.; Terryn, H., A Generalized Electrochemical Aggregative Growth Mechanism. *J. Am. Chem. Soc.* **2013,** *135*, 11550-11561.
(8) Harniman, R. L.; Plana, D.; Carter, G. H.; Bradley, K. A.; Miles, M. J.; Fermín, D. J., Real-Time Tracking of Metal Nucleation *via* Local Perturbation of Hydration Layers. *Nature Communications* **2017,** *8*, 1-8.
(9) Milchev, A.; Stoyanov, S., Classical and Atomistic Models of Electrolytic Nucleation: Comparison with Experimental Data. *Journal of Electroanalytical Chemistry and Interfacial Electrochemistry* **1976,** *72*, 33-43.
(10) Budevski, E.; Staikov, G.; Lorenz, W. J., Electrocrystallization: Nucleation and Growth Phenomena. *Electrochim. Acta* **2000,** *45*, 2559-2574.
(11) Scharifker, B. R.; Mostany, J., Electrochemical Nucleation and Growth. In *Encyclopedia of Electrochemistry*, Bard, A. J.; Stratmann, M., Eds. Wiley-VCH: Germany, 2007; Vol. 1, pp 512-534.
(12) Williamson, M. J.; Tromp, R. M.; Vereecken, P. M.; Hull, R.; Ross, F. M., Dynamic Microscopy of Nanoscale Cluster Growth at the Solid-Liquid Interface. *Nat. Mater.* **2003,** *2*, 532-536.
(13) Radisic, A.; Vereecken, P. M.; Hannon, J. B.; Searson, P. C.; Ross, F. M., Quantifying Electrochemical Nucleation and Growth of Nanoscale Clusters Using Real-Time Kinetic Data. *Nano Lett.* **2006,** *6*, 238-242.
(14) Velmurugan, J.; Noël, J.-M.; Nogala, W.; Mirkin, M. V., Nucleation and Growth of Metal on Nanoelectrodes. *Chemical Science* **2012,** *3*, 3307-3314.

(15) Lai, S. C. S.; Lazenby, R. A.; Kirkman, P. M.; Unwin, P. R., Nucleation, Aggregative Growth and Detachment of Metal Nanoparticles During Electrodeposition at Electrode Surfaces. *Chemical Science* **2015,** *6*, 1126-1138.
(16) Kim, Y.-R.; Lai, S. C. S.; McKelvey, K.; Zhang, G.; Perry, D.; Miller, T. S.; Unwin, P. R., Nucleation and Aggregative Growth of Palladium Nanoparticles on Carbon Electrodes: Experiment and Kinetic Model. *The Journal of Physical Chemistry C* **2015,** *119*, 17389-17397.
(17) Matsushima, H.; Lin, S. W.; Morin, S.; Magnussen, O. M., *In Situ* Video-STM Studies of the Mechanisms and Dynamics of Electrochemical Bismuth Nanostructure Formation on Au. *Faraday Discuss.* **2016,** *193*, 171-185.
(18) Ross, F. M., Opportunities and Challenges in Liquid Cell Electron Microscopy. *Science* **2015,** *350*, aaa98861-aaa98869.
(19) Hodnik, N.; Dehm, G.; Mayrhofer, K. J. J., Importance and Challenges of Electrochemical *in Situ* Liquid Cell Electron Microscopy for Energy Conversion Research. *Acc. Chem. Res.* **2016,** *49*, 2015-2022.
(20) Li, Z. Y.; Young, N. P.; Di Vece, M.; Palomba, S.; Palmer, R. E.; Bleloch, A. L.; Curley, B. C.; Johnston, R. L.; Jiang, J.; Yuan, J., Three-Dimensional Atomic-Scale Structure of Size-Selected Gold Nanoclusters. *Nature* **2007,** *451*, 46.
(21) Milchev, A.; Stoyanov, S.; Kaischev, R., Atomistic Theory of Electrolytic Nucleation: I. *Thin Solid Films* **1974,** *22*, 255-265.
(22) Milchev, A.; Malinowski, J., Phase Formation - Stability and Nucleation Kinetics of Small Clusters. *Surf. Sci.* **1985,** *156*, 36-43.
(23) Liu, Y.; Gokcen, D.; Bertocci, U.; Moffat, T. P., Self-Terminating Growth of Platinum Films by Electrochemical Deposition. *Science* **2012,** *338*, 1327-1330.
(24) Zhou, M.; Dick, J. E.; Bard, A. J., Electrodeposition of Isolated Platinum Atoms and Clusters on Bismuth-Characterization and Electrocatalysis. *J. Am. Chem. Soc.* **2017,** *139*, 17677-17682.
(25) Mayrhofer, K. J. J.; Meier, J. C.; Ashton, S. J.; Wiberg, G. K. H.; Kraus, F.; Hanzlik, M.; Arenz, M., Fuel Cell Catalyst Degradation on the Nanoscale. *Electrochem. Commun.* **2008,** *10*, 1144-1147.
(26) Ustarroz, J.; Gupta, U.; Hubin, A.; Bals, S.; Terryn, H., Electrodeposition of Ag Nanoparticles onto Carbon Coated TEM Grids: A Direct Approach to Study Early Stages of Nucleation. *Electrochem. Commun.* **2010,** *12*, 1706-1709.
(27) Macpherson, J. V., A Practical Guide to Using Boron Doped Diamond in Electrochemical Research. *Phys. Chem. Chem. Phys.* **2015,** *17*, 2935-2949.
(28) Klein, R. K.; Kephart, J. O.; Pantell, R. H.; Park, H.; Berman, B. L.; Swent, R. L.; Datz, S.; Fearick, R. W., Electron Channeling Radiation from Diamond. *Physical Review B* **1985,** *31*, 68-92.
(29) Shinotsuka, H.; Tanuma, S.; Powell, C. J.; Penn, D. R., Calculations of Electron Inelastic Mean Free Paths. X. Data for 41 Elemental Solids Over the 50 eV to 200 keV Range with the Relativistic Full Penn Algorithm. *Surf. Interface Anal.* **2015,** *47*, 871-888.
(30) Milchev, A.; Stoyanov, S.; Kaischev, R., Atomistic Theory of Electrolytic Nucleation: II. *Thin Solid Films* **1974,** *22*, 267-274.
(31) Moffat, T. P., Electrodeposition of $Ni_{1-x}Al_x$ in a Chloroaluminate Melt. *J. Electrochem. Soc.* **1994,** *141*, 3059-3070.
(32) Wild, C.; Herres, N.; Koidl, P., Texture Formation in Polycrystalline Diamond Films. *J. Appl. Phys.* **1990,** *68*, 973-978.

(33) Blum, V.; Gehrke, R.; Hanke, F.; Havu, P.; Havu, V.; Ren, X.; Reuter, K.; Scheffler, M., Ab Initio Molecular Simulations with Numeric Atom-Centered Orbitals. *Comput. Phys. Commun.* **2009,** *180*, 2175-2196.
(34) LeBeau, J. M.; Findlay, S. D.; Allen, L. J.; Stemmer, S., Quantitative Atomic Resolution Scanning Transmission Electron Microscopy. *Phys. Rev. Lett.* **2008,** *100*, 2061011-2061014.
(35) Fujita, T.; Guan, P.; McKenna, K.; Lang, X.; Hirata, A.; Zhang, L.; Tokunaga, T.; Arai, S.; Yamamoto, Y.; Tanaka, N.; Ishikawa, Y.; Asao, N.; Yamamoto, Y.; Erlebacher, J.; Chen, M., Atomic Origins of the High Catalytic Activity of Nanoporous Gold. *Nat. Mater.* **2012,** *11*, 775-780.
(36) Redmond, P. L.; Hallock, A. J.; Brus, L. E., Electrochemical Ostwald Ripening of Colloidal Ag Particles on Conductive Substrates. *Nano Lett.* **2005,** *5*, 131-135.
(37) Ouyang, R.; Liu, J.-X.; Li, W.-X., Atomistic Theory of Ostwald Ripening and Disintegration of Supported Metal Particles under Reaction Conditions. *J. Am. Chem. Soc.* **2013,** *135*, 1760-1771.
(38) Zhu, C.; Fu, S.; Shi, Q.; Du, D.; Lin, Y., Single-Atom Electrocatalysts. *Angewandte Chemie International Edition* **2017,** *56*, 13944-13960.
(39) Gambardella, P.; Rusponi, S.; Veronese, M.; Dhesi, S. S.; Grazioli, C.; Dallmeyer, A.; Cabria, I.; Zeller, R.; Dederichs, P. H.; Kern, K.; Carbone, C.; Brune, H., Giant Magnetic Anisotropy of Single Cobalt Atoms and Nanoparticles. *Science* **2003,** *300*, 1130-1133.
(40) Seh, Z. W.; Kibsgaard, J.; Dickens, C. F.; Chorkendorff, I.; Norskov, J. K.; Jaramillo, T. F., Combining Theory and Experiment in Electrocatalysis: Insights into Materials Design. *Science* **2017,** *355*, 1-12.
(41) Hutton, L. A.; Iacobini, J. G.; Bitziou, E.; Channon, R. B.; Newton, M. E.; Macpherson, J. V., Examination of the Factors Affecting the Electrochemical Performance of Oxygen-Terminated Polycrystalline Boron-Doped Diamond Electrodes. *Anal. Chem.* **2013,** *85*, 7230-7240.
(42) Hussein, H. E. M.; Amari, H.; Macpherson, J. V., Electrochemical Synthesis of Nanoporous Platinum Nanoparticles Using Laser Pulse Heating: Application to Methanol Oxidation. *ACS Catalysis* **2017,** *7*, 7388-7398.
(43) Perdew, J. P.; Burke, K.; Ernzerhof, M., Generalized Gradient Approximation Made Simple. *Phys. Rev. Lett.* **1996,** *77*, 3865-3868.
(44) Tkatchenko, A.; Scheffler, M., Accurate Molecular Van Der Waals Interactions from Ground-State Electron Density and Free-Atom Reference Data. *Phys. Rev. Lett.* **2009,** *102*, 0730051-0730054.
(45) Bahn, S. R.; Jacobsen, K. W., An Object-Oriented Scripting Interface to a Legacy Electronic Structure Code. *Computing in Science & Engineering* **2002,** *4*, 56-66.
(46) Henkelman, G.; Uberuaga, B. P.; Jónsson, H., A Climbing Image Nudged Elastic Band Method for Finding Saddle Points and Minimum Energy Paths. *The Journal of Chemical Physics* **2000,** *113*, 9901-9904.
(47) Goedecker, S., Minima Hopping: An Efficient Search Method for the Global Minimum of the Potential Energy Surface of Complex Molecular Systems. *The Journal of Chemical Physics* **2004,** *120*, 9911-9917.
(48) Peterson, A. A., Global Optimization of Adsorbate–Surface Structures While Preserving Molecular Identity. *Top. Catal.* **2014,** *57*, 40-53.